Engineered far-fields of metal-metal terahertz quantum cascade lasers with integrated planar horn structures

F. Wang,[1,*] I. Kundu,[2] L. Chen,[2] L. Li,[2] E. H. Linfield,[2] A. G. Davies,[2] S. Moumdji,[3] R. Colombelli,[3] J. Mangeney,[1] J. Tignon,[1] and S. S. Dhillon[1]

[1]*Laboratoire Pierre Aigrain, Ecole Normale Supérieure-PSL Research University, CNRS, Université Pierre et Marie Curie-Sorbonne Universités, Université Paris Diderot-Sorbonne Paris Cité, 75231 Paris, France*
[2]*School of Electronic and Electrical Engineering, University of Leeds, Leeds LS9 2JT, United Kingdom*
[3]*Institut d'Electronique Fondamentale, Université Paris Sud, UMR8622 CNRS, 91405 Orsay, France*
[*]*feihu.wang@lpa.ens.fr*

Abstract: The far-field emission profile of terahertz quantum cascade lasers (QCLs) in metal-metal waveguides is controlled in directionality and form through planar horn-type shape structures, whilst conserving a broad spectral response. The structures produce a gradual change in the high modal confinement of the waveguides and permit an improved far-field emission profile and resulting in a four-fold increase in the emitted output power. The two-dimensional far-field patterns are measured at 77 K and are agreement in with 3D modal simulations. The influence of parasitic high-order transverse modes is shown to be controlled by engineering the horn structure (ridge and horn widths), allowing only the fundamental mode to be coupled out.

OCIS codes: (140.0140) Lasers and laser optics; (140.5965) Semiconductor lasers, quantum cascade.

References and links

1. R. Köhler, A. Tredicucci, F. Beltram, H. E. Beere, E. H. Linfield, A. G. Davies, D. A. Ritchie, R. C. Iotti, and F. Rossi, "Terahertz semiconductor-heterostructure laser," Nature **417**(6885), 156–159 (2002).
2. S. Fathololoumi, E. Dupont, C. W. I. Chan, Z. R. Wasilewski, S. R. Laframboise, D. Ban, A. Mátyás, C. Jirauschek, Q. Hu, and H. C. Liu, "Terahertz quantum cascade lasers operating up to ~ 200 K with optimized oscillator strength and improved injection tunneling," Opt. Express **20**(4), 3866–3876 (2012).
3. W. Maineult, P. Gellie, A. Andronico, P. Filloux, G. Leo, C. Sirtori, S. Barbieri, E. Peytavit, T. Akalin, J.-F. Lampin, H. E. Beere, and D. A. Ritchie, "Metal-metal terahertz quantum cascade laser with micro-transverse-electromagnetic-horn antenna," Appl. Phys. Lett. **93**(18), 183508 (2008).
4. L. Li, L. Chen, J. Zhu, J. Freeman, P. Dean, A. Valavanis, A. G. Davies, and E. H. Linfield, "Terahertz quantum cascade lasers with> 1 W output powers," Electron. Lett. **50**(4), 309–311 (2014).
5. G. Xu, R. Colombelli, S. P. Khanna, A. Belarouci, X. Letartre, L. Li, E. H. Linfield, A. G. Davies, H. E. Beere, and D. A. Ritchie, "Efficient power extraction in surface-emitting semiconductor lasers using graded photonic heterostructures," Nat. Commun. **3**, 952 (2012).
6. J. A. Fan, M. A. Belkin, F. Capasso, S. Khanna, M. Lachab, A. G. Davies, and E. H. Linfield, "Surface emitting terahertz quantum cascade laser with a double-metal waveguide," Opt. Express **14**(24), 11672–11680 (2006).
7. M. I. Amanti, M. Fischer, G. Scalari, M. Beck, and J. Faist, "Low-divergence single-mode terahertz quantum cascade laser," Nat. Photonics **3**(10), 586–590 (2009).
8. M. Wienold, B. Röben, L. Schrottke, R. Sharma, A. Tahraoui, K. Biermann, and H. T. Grahn, "High-temperature, continuous-wave operation of terahertz quantum-cascade lasers with metal-metal waveguides and third-order distributed feedback," Opt. Express **22**(3), 3334–3348 (2014).
9. J. R. Freeman, J. Maysonnave, H. E. Beere, D. A. Ritchie, J. Tignon, and S. S. Dhillon, "Electric field sampling of modelocked pulses from a quantum cascade laser," Opt. Express **21**(13), 16162–16169 (2013).
10. J. Maysonnave, K. Maussang, J. R. Freeman, N. Jukam, J. Madéo, P. Cavalié, R. Rungsawang, S. P. Khanna, E. H. Linfield, A. G. Davies, H. E. Beere, D. A. Ritchie, S. S. Dhillon, and J. Tignon, "Mode-locking of a terahertz laser by direct phase synchronization," Opt. Express **20**(19), 20855–20862 (2012).

#254740 Received 7 Dec 2015; revised 15 Jan 2016; accepted 15 Jan 2016; published 27 Jan 2016

11. S. Barbieri, M. Ravaro, P. Gellie, G. Santarelli, C. Manquest, C. Sirtori, S. P. Khanna, E. H. Linfield, and A. G. Davies, "Coherent sampling of active mode-locked terahertz quantum cascade lasers and frequency synthesis," Nat. Photonics **5**(5), 306–313 (2011).
12. D. Burghoff, T.-Y. Kao, N. Han, C. W. I. Chan, X. Cai, Y. Yang, D. J. Hayton, J.-R. Gao, J. L. Reno, and Q. Hu, "Terahertz laser frequency combs," Nat. Photonics **8**(6), 462–467 (2014).
13. D. Burghoff, T.-Y. Kao, D. Ban, A. W. M. Lee, Q. Hu, and J. Reno, "A terahertz pulse emitter monolithically integrated with a quantum cascade laser," Appl. Phys. Lett. **98**(6), 061112 (2011).
14. M. C. Wanke, C. Nordquist, C. L. Arrington, A. M. Rowen, A. D. Grine, E. A. Shaner, and M. Lee, "Integration of terahertz quantum cascade lasers with lithographically micromachined waveguides," in *33rd International Conference on Infrared, Millimeter and Terahertz Waves* (2008), pp. 15–19.
15. A. Brewer, J. R. Freeman, P. Cavalié, J. Maysonnave, J. Tignon, S. S. Dhillon, H. E. Beere, and D. A. Ritchie, "Coherent detection of metal-metal terahertz quantum cascade lasers with improved emission characteristics," Appl. Phys. Lett. **104**(8), 081107 (2014).
16. D. Oustinov, N. Jukam, R. Rungsawang, J. Madéo, S. Barbieri, P. Filloux, C. Sirtori, X. Marcadet, J. Tignon, and S. Dhillon, "Phase seeding of a terahertz quantum cascade laser," Nat. Commun. **1**(6), 69 (2010).
17. M. A. Belkin, J. A. Fan, S. Hormoz, F. Capasso, S. P. Khanna, M. Lachab, A. G. Davies, and E. H. Linfield, "Terahertz quantum cascade lasers with copper metal-metal waveguides operating up to 178 K," Opt. Express **16**(5), 3242–3248 (2008).
18. F. Hyo and J. Eom, *Electromagnetic Wave Theory for Boundary-Value Problems: An Advanced Course on Analytical Methode* (Springer, 2004), Ch. 3.
19. P. Gellie, W. Maineult, A. Andronico, G. Leo, C. Sirtori, S. Barbieri, Y. Chassagneux, J. R. Coudevylle, R. Colombelli, S. P. Khanna, E. H. Linfield, and A. G. Davies, "Effect of transverse mode structure on the far field pattern of metal-metal terahertz quantum cascade lasers," J. Appl. Phys. **104**(12), 124513 (2008).
20. F. Wang, K. Maussang, S. Moumdji, R. Colombelli, J. R. Freeman, I. Kundu, L. Li, E. H. Linfield, A. G. Davies, J. Mangeney, J. Tignon, and S. S. Dhillon, "Generating ultrafast pulses of light from quantum cascade lasers," Optica **2**(11), 944 (2015).

1. Introduction

Terahertz (THz) frequency quantum cascade lasers (QCLs) are semiconductor sources based on intersubband transitions and permit laser emission over a wide portion of the THz spectrum. THz QCLs have undergone considerable improvements in operation since their first demonstration [1], especially in terms of the achievable output power and operating temperature. However, typically these two parameters cannot be optimized simultaneously in a given QCL device. The highest temperature operation of 200 K [2] has been demonstrated through use of metal-metal (MM) waveguides, where a high modal gain is achieved through the high modal confinement. However, a consequence of this is a highly diffracted beam and a large facet reflectivity leading to weak directionality and low output powers [3], respectively. The use of single plasmon based waveguides, on the other hand, have been shown to lead to output power of up to 1 W [4] but such QCLs are typically limited to operation at temperatures below 77 K.

Several monolithic methods have been proposed and realized to address this problem based on photonic structures for surface emission [5,6]. Other powerful demonstrations have exploited 3rd order gratings for emission along the ridge length [7,8]. Although these techniques can extract the QCL power and engineer the far-field emission profile efficiently, they are inherently mono-frequency and not suitable for broadband emission that would be of interest to modelocking [9–11] or frequency comb [12] generation applications. Most broadband methods, however, have relied on manual positioning of external elements such as silicon lenses placed on the facet [13], suspended antenna structures [3] or rectangular waveguides [14]. Owing to the manual nature, the techniques have proved to be difficult or non-reproducible when thermally cycled.

A promising technique has been recently demonstrated in which planar horn-like structures (PHSs) are etched into the QCL surface metal layer, so that the confined mode is better matched to a radiative mode [15]. This simple approach has led to a considerable improvement in directionality and output power without significantly affecting the QCL temperature performance, and has proven to be stable. Indeed injection seeding [16] of bound-to-continuum QCLs with PHS have been recently demonstrated [15]. However, no control of the far-field profile was demonstrated with only one-dimensional profiles of the far-field

#254740 Received 7 Dec 2015; revised 15 Jan 2016; accepted 15 Jan 2016; published 27 Jan 2016

measured. Further the emitted spectrum from the PHS was not shown to be broadband owing to the use of low spectral bandwidth active regions. In this work, we demonstrate how the far-field emission profile can be controlled by engineering the QCL's transverse modes and the geometry of the PHS, as well as showing the broadband nature of the emission. We further show two-dimensional far-field patterns that are in good agreement with electromagnetic simulations.

2. Experiments

QCLs with a central frequency at 3.1 THz and a spectral bandwidth of 0.6 THz were used, employing an active region design based on longitudinal optical phonon depopulation [17]. These designs have the highest temperature operation when placed in a MM waveguide, and allowed the QCL to be operated at liquid nitrogen temperatures. The designs also possess an inherently large gain bandwidth, ideal in illustrating the broadband nature of the PHS. The growth was performed using molecular beam epitaxy followed by wafer bonding onto a host GaAs wafer. The original substrate was removed by a combination of mechanical and chemical techniques. The entire doped layer, as well as the etch-stop layer, was removed, reducing the waveguide losses. The MM wafers were then processed with laser ridge widths of 40 μm, 60 μm and 80 μm, and cleaved into cavity lengths of 3 mm, 2 mm and 3 mm, respectively.

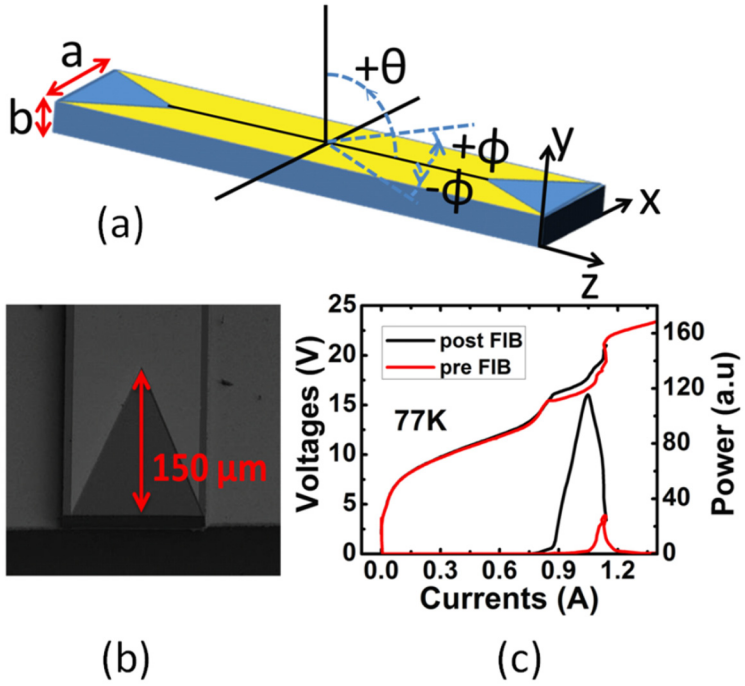

Fig. 1. (a) Schematic of metal-metal THz QCLs with ~150-μm-long triangle horn structures at each end of the QCL cavity. (b) SEM image of a horn structure on one end of the QCL. (c) The L-I-V curves at 77 K pre- and post-FIB milling of horn structures.

The PHS were realized by post processing through the use of focused ion beam (FIB) milling to remove the top metal layer as shown in Figs. 1(a) and 1(b). This allows the strongly confined mode to gradually adapt into a propagating beam, reducing the facet reflectivity, and therefore resulting in a higher output power and a directional far-field. Generally, the longer the horn length, the larger the output power and the more directional the beam. However, a

#254740 Received 7 Dec 2015; revised 15 Jan 2016; accepted 15 Jan 2016; published 27 Jan 2016

long PHS results in higher effective mirror losses and an increase in laser threshold, as detailed in ref [15]. A horn length of 150 µm was chosen here as a compromise.

Figure 1(c) shows the output light-current-voltage characteristics of an 80-µm-wide ridge pre- and post-FIB milling, with the QCL at 77 K. The QCL was operated in pulsed mode with 500-ns-long electrical pulses at a repetition frequency of 50 kHz. A 20 Hz electrical envelope modulation was used to enable lock-in detection of the output power using a Golay cell detector. A f/1.67 parabolic mirror was used to collect the output radiation from the QCL, and a f/2 parabolic mirror used to focus it onto the Golay cell. A factor of four increase in measured output power was observed for the QCL incorporating the horn (post FIB). This increase is partly due to a reduced facet reflectivity. The threshold currents of the pre- and post-FIB sample (from the change in differential resistance in the V-I curve) are 0.849 A and 0.875 A, respectively, corresponding to a reduction in reflectivity from approximately 0.8 to 0.65, respectively, with a calculated waveguide loss of 22 cm^{-1} (see below). This reduction in reflectivity would only result in a two-fold increase in output power, and so does not account for the four-fold increase observed. (The L-I was not used to determine the threshold owing to an small overshoot in time of the electrical characteristics, resulting in the threshold in the light emission appearing smaller for the horn antenna sample. The V-I is taken over a large time window that does not include the electrical overshoot and is therefore more robust to determine the laser threshold).

We show below that this difference arises from there being a more directional beam in the devices with horn-like structures. We also demonstrate that the far-field profile can be engineered by controlling the transverse mode that propagates through the QCL waveguide. Indeed, by favouring the fundamental transverse mode, we demonstrate that the far-field profile can be changed from a double to a single lobed emission. The far-fields profile of three samples were measured and simulated; an 80-µm and a 40-µm-wide ridge each with a PHS, and a 60-µm-wide ridge as cleaved.

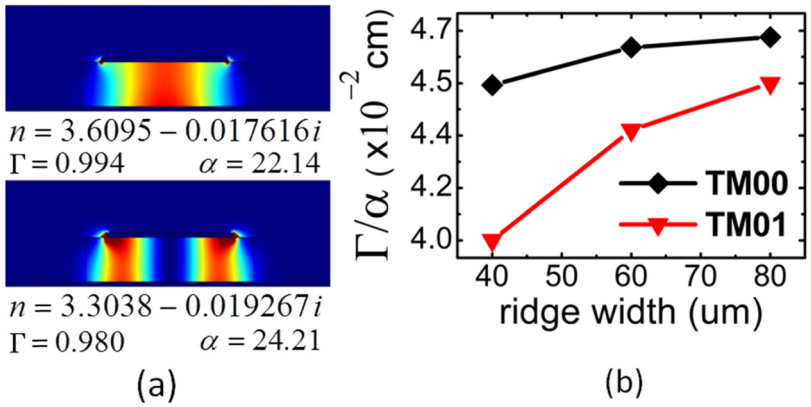

Fig. 2. (a) Modal simulations of the fundamental TM_{00} (top) and second order mode TM_{01} (bottom) for a 40-µm-width metal-metal QCL. (b) The figure of merit, Γ/α, as a function of QCL ridge width for the fundamental TM_{00} (black) and second order mode TM_{01} (red).

The effect of the ridge width can be seen by analyzing the modes that are permitted to propagate. For the general case of a waveguide of width a and height b (see Fig. 1(a)) with no loss, the propagation constant, β, is given by [18]:

$$\beta = \sqrt{k^2 - (k_x^2 + k_y^2)} = \sqrt{\omega^2 n^2 \mu\varepsilon - (k_x^2 + k_y^2)} \qquad (1)$$

#254740 Received 7 Dec 2015; revised 15 Jan 2016; accepted 15 Jan 2016; published 27 Jan 2016

where n is the refractive index, ω is the angular frequency, and $k_x = m\pi/a$ and $k_y = 1\pi/b$ are the wavevectors in the x and y directions with propagation in the z-direction. (m and l are the integer mode numbers). For a mode to propagate, $\beta^2 > 0$ and therefore:

$$(k_x^2 + k_y^2) < \omega^2 n^2 \mu\varepsilon \rightarrow (\frac{\pi m}{a})^2 + (\frac{\pi 1}{b})^2 < \omega^2 n^2 \mu\varepsilon \tag{2}$$

For intersubband transitions, the electric field polarization is perpendicular to the laser surface (transverse magnetic (TM)), and with $b < a$ ($l = 0$):

$$m < \frac{\omega a n}{\pi}\sqrt{\mu\varepsilon} = 2a\, nf\sqrt{\mu\varepsilon} = \frac{2an}{\lambda} \tag{3}$$

where λ is the wavelength. From Eq. (3) it can be seen that the number of transverse modes can be limited by reducing the ridge width a. For example, choosing a ridge less than 30 μm will result in only the fundamental transverse mode $TM_{0,0}$ propagating.

To take into account the actual QCL structure with optical losses, simulations of the 2D waveguide modes were performed (COMSOL). Figure 2(a) shows the mode profiles of the fundamental (TM_{00}) and second order mode (TM_{01}) at 3 THz for a 40-μm-wide ridge. The modal overlap with the active region, Γ, and the waveguide losses, α, are found to be 0.994 and 22cm^{-1}, and 0.98 and 24cm^{-1}, for the TM_{00} and TM_{01} modes, respectively. The modal overlap is smaller for higher order modes owing to a larger overlap with the surrounding air, and the losses increase owing to a larger overlap with the surrounding metal layers. This results in a reduction in the figure of merit, Γ/α, for higher order modes, which indicates that they are less likely to demonstrate laser action. This is summarized in Fig. 2(b) that shows the figure of merit as a function of ridge width, highlighting that the difference in the figure of merit between the fundamental and second order mode increases as the ridge width decreases.

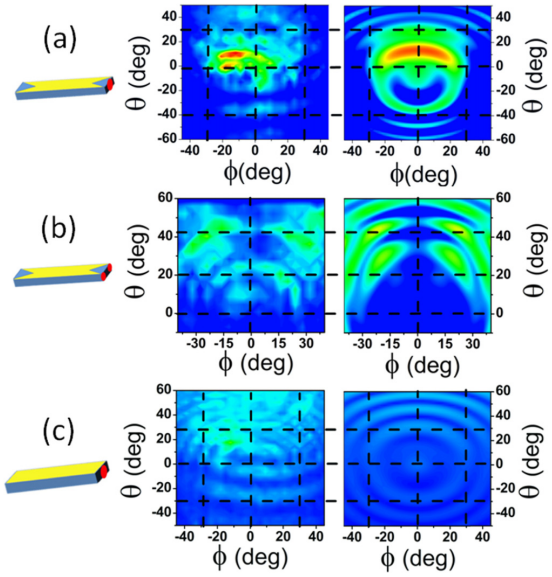

Fig. 3. Simulated (right) and measured (left) far-field patterns of metal-metal THz QCLs with different waveguide structures. (a) 3-mm-long 40-μm-wide metal-metal THz QCL with 150-μm-long PHS. (b) 3-mm-long 80-μm-wide metal-metal THz QCL with 150-μm-long PHS. (c) 2-mm-long 60-μm-wide metal-metal THz QCL without any planar horn structure. The measurements were all taken at 77 K.

#254740 Received 7 Dec 2015; revised 15 Jan 2016; accepted 15 Jan 2016; published 27 Jan 2016

To simulate the effect of the PHS on the far field, 3D modal simulations were performed using a finite element analysis (RF module). Here, the transverse modes were simulated in MM THz QCLs with a planar horn structure on the top metal layer. The QCLs was modelled in three parts: 1. Top metal gold waveguide layer (2 µm thick) with two 150-µm-long triangle horn shapes on each end of the laser; 2. The active medium layer (10 µm thick GaAs). 3. Bottom gold metal layer (2 µm thick). The model was placed in an air sphere to determine the far-field profile using a $TM_{0,0}$ source to excite the transverse modes within the cavities at one end of the ridge. (See appendix for further details).

The measured and calculated far-field profiles corresponding to the transverse modes are shown in Fig. 3 (left and right side of figure, respectively). The measurements were performed with a Golay detector rotated around the QCL central axis [19]. In all cases the QCL was operated at a temperature of 77 K. Figures 3(a) and 3(b) show the far-field patterns of a 40-µm- and 80-µm-wide MM THz QCLs with planar horn structures, respectively. Figure 3(c) shows the far-field profile from a QCL with an un-patterned ridge of width 60 µm. The simulations and measurements are in good agreement, and demonstrate the effect of increasing the ridge width. As mentioned above, in the 40-µm-wide cavity, only the fundamental mode $TM_{0,0}$ is present and results in a single lobed far-field profile. Compared to the 60-µm-wide un-patterned QCL (Fig. 3(c)), the far-field profile is less diffracted with the power concentrated at $\theta = 10^{\circ}$ and $\phi = 15^{\circ}$ (The slight difference in angle in the ϕ plane when compared to the simulations was a result of the QCL being mounted at a small angle on the cryostat cold finger). In the case of the 80 µm ridge with a horn structure, the QCL demonstrates laser action on a higher order mode ($TM_{0,1}$) that, as a consequence, results in a considerably different far-field profile. Indeed the far-field shows a more diffracted double lobe pattern with $\theta = 43^{\circ}$ and $\phi = \pm 25^{\circ}$ in agreement with the simulated profile. Figure 3(c) shows the far-field patterns of the 60-µm-wide MM THz QCL without an PHS and is typical of a standard MM QCL with a highly diffractive beam and a concentric ring profile [3] owing to the tight sub-wavelength confinement of the mode.

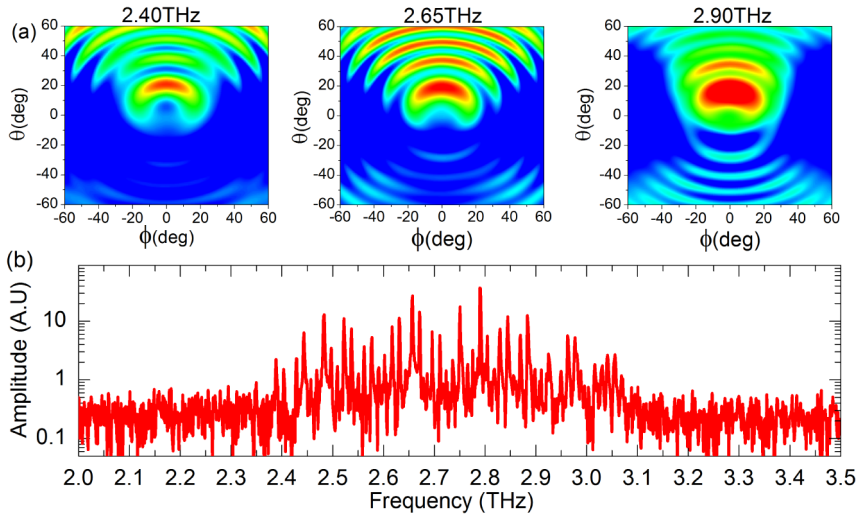

Fig. 4. (a) Simulated far field profiles at 2.4 THz, 2.65 THz and 2.9 THz for QCL with central emission frequency of ~2.7 THz with a PHS of length 150 µm. (b) The measured spectrum taken at 10K showing a broadband response.

Although the 60-µm-wide ridge can permit propagation of higher order modes, the QCL far field appears to be a result of just the $TM_{0,0}$ mode, suggesting that the ridge is small enough to still favor the fundamental mode only. Although the ridge widths are different, the

#254740 Received 7 Dec 2015; revised 15 Jan 2016; accepted 15 Jan 2016; published 27 Jan 2016

2-mm-long 60-µm-wide QCL ridge has the same volume as the 3-mm-long 40-µm-wide ridge and so should have comparable output powers, which allows the effect of the horn to be determined. From the measured far-field profiles, the maximum power output of the horn coupled QCL is ~3 times greater than that of the QCL with no horn. The simulations, however, show a five-fold increase. The discrepancy could be a result of imperfections in the horn fabrication where the FIB milling can leave small metallic defects on the surface or on the quality of the cleaved facet.

From the far-fields profiles, the collection efficiency of the parabolic mirror used for the acquisition of the output power of Fig. 1 was determined. A horn coupled QCL would collect 28% of the total power emitted by the QCL while for the as-cleaved device, this falls to 16%. This adds to the reduction in reflectivity highlighted above for higher output power and explains the four-fold increase in power observed in Fig. 1.

To illustrate the broadband spectral nature of the PHS, the spectrum of a QCL operating with a similar active region but operating around 2.7 THz with a bandwidth of ~600 GHz [20] was investigated. The sample ridge width here was 60 µm with a cavity length of 3mm and the PHS length was 150 µm. The calculated far-fields for 2.4 THz, 2.65 THz and 2.9 THz are shown in Fig. 4(a). Although there is a slight dependence on the frequency with a larger divergence and more elliptical field for the lower frequencies, all the far fields show a similar single lobed far field. Figure 4(b) shows the resulting spectrum using an injection seeding technique [16] which shows that emission extends from 2.4 THz to 3 THz. Although there appears to be a stronger distribution in intensities of the Fabry-Perot modes when compared to the as cleaved device [20], a similar bandwidth is obtained illustrating the broad spectral response of the PHS.

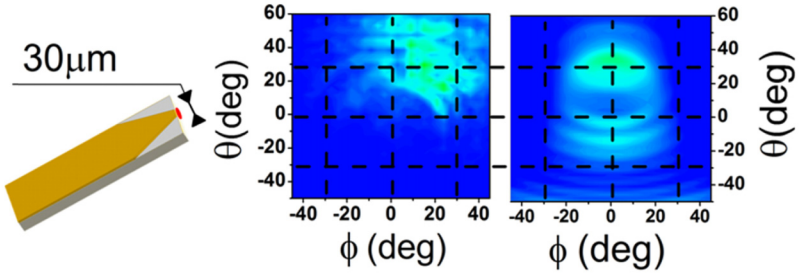

Fig. 5. Simulated (right) and measured (left) far-field patterns of a 3-mm-long 80-µm-wide metal-metal THz QCLs with a 250-µm-long inverse planar horn structures. The measurements were all taken at 77 K.

As can be observed from Fig. 3, although larger output powers can be achieved, a large ridge with a PHS results in a double lobed far-field, which is not ideal for applications. To circumvent this, a tapered shape was realized on the end of the QCL. Here, rather than removing the metal layer from the centre of the ridge, the metal layer was selectively removed from edges of an 80-µm-wide ridge to a 30 µm point at the QCL facet over a taper length of 250 µm (see Fig. 5). This scheme increases the losses of the higher order modes and therefore limits laser action to the fundamental mode. Figure 5 shows the measured and simulated far field profiles for an 80-µm-wide ridge. The far field is improved considerably and, in contrast to Fig. 4(b), is single lobed. (The slight angle in $\phi = 18^{\circ}$ in the measurement data is a result of a slight asymmetry in the realized PHS fabrication). This shows that the PHS shape can be adapted to the ridge width and not is limited to small ridge widths for lasing on the fundamental mode.

#254740 Received 7 Dec 2015; revised 15 Jan 2016; accepted 15 Jan 2016; published 27 Jan 2016

3. Conclusion

In conclusion, the application of a broadband PHS to MM THz QCLs has been demonstrated and the ridge width engineered to favor single lobed emission in the far field. All measurements were performed at temperatures and electrical power dissipation compatible with liquid nitrogen cooling or cryocooler temperatures. The 150-µm-long planar horn structures integrated onto the top metal surface of the QCL reduces the reflectivity and improves the quality of the far-field profiles. This permits a four-fold increase in the detected power whilst conserving a broad spectral response. Further, with longer PHS lengths, the output powers and directionality can be increased considerably further. This stability and the inherent broadband nature of these structures will allow these devices to be employed for applications such as injection seeding of QCLs for coherent detection and the generation of high power frequency combs.

Appendix A: Transverse mode simulations for different ridge width

The far field was simulated using a finite element analysis (RF module). Here, the transverse modes were simulated in MM THz QCLs with a planar horn structure on the top metal layer. The QCLs was modelled with a top metal gold waveguide layer (2 µm thick) with two 150-µm-long triangle horn shapes on each end of the laser, the active medium layer (10 µm thick GaAs) and the bottom gold metal layer (2 µm thick). The model was placed in an air sphere to determine the far-field profile with an appropriate mesh as shown in Fig. 6. A $TM_{0,0}$ source is employed to excite the transverse modes within the cavities at one end of the ridge (right side of the cavities in Fig. 7). Figures 7(a)-7(c) shows the resulting simulations of the ridge width on the transverse modes for ridge widths of 40 µm, 60 µm, and 80 µm. For the 40-µm-wide cavity, although the $TM_{0,1}$ mode begins to appear, the fundamental $TM_{0,0}$ mode still dominates. Further increases in the ridge width results in the stronger appearance of other high order transverse modes.

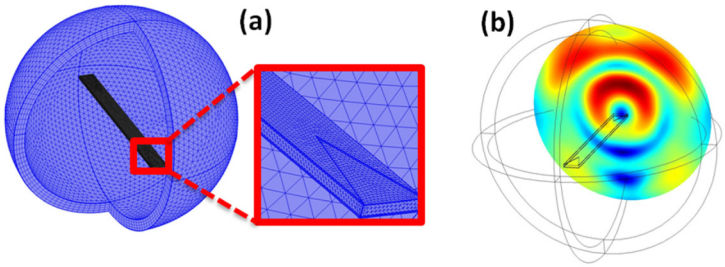

Fig. 6. (a) Mesh used in air-field and QCL ridge to determine the far field emitted from the QCL. (b) Example of simulated far field projected on the air-sphere.

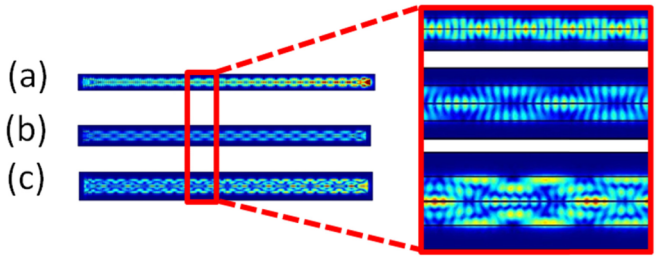

Fig. 7. Top view of QCL showing transverse modes excited by a $TM_{0,0}$ excitation on the right side of the ridge for 3-mm-long cavities with 150-µm-long planar triangle structures on the top metal layer on both facets. (a) Ridge width = 40 µm. (b) Ridge width = 60 µm. (c) Ridge width = 80 µm.

#254740 Received 7 Dec 2015; revised 15 Jan 2016; accepted 15 Jan 2016; published 27 Jan 2016

Acknowledgments

This project has received funding from the European Union's Horizon 2020 research and innovation programme under grant agreement No 665158, the French National Research Agency (ANR-12-NANO-0014 "PhaseLock"), the EPSRC (UK), the EC programme (TOSCA), and the Royal Society and Wolfson Foundation. The device fabrication has been performed at the nano-center CTU-IEF-Minerve, which was partially funded by the Conseil Général de l'Essonne.

#254740 Received 7 Dec 2015; revised 15 Jan 2016; accepted 15 Jan 2016; published 27 Jan 2016